

# Spectral Variation of the Hard X-ray Emission from the Crab Nebula with the Suzaku Hard X-ray Detector

Tomomi KOUZU,<sup>1</sup> Makoto S. TASHIRO,<sup>1</sup> Yukikatsu TERADA,<sup>1</sup> Shin'ya YAMADA,<sup>2</sup> Aya BAMBA,<sup>3</sup> Teruaki ENOTO,<sup>2</sup>  
Koji MORI,<sup>4</sup> Yasushi FUKAZAWA<sup>5</sup> and Kazuo MAKISHIMA<sup>6</sup>

<sup>1</sup> Graduate School of Science and Engineering, Saitama University, Shimo-Okubo 255, Sakura, Saitama 338-8570, Japan

<sup>2</sup> High Energy Astrophysics Laboratory, Institute of Physical and Chemical Research (RIKEN), 2-1 Hirosawa, Wako, Saitama 351-0198, Japan

<sup>3</sup> Graduate School of Science and Engineering, Aoyama-Gakuin University, 5-10-1 Fuchinobe, Chuo, Sagami-hara, Kanagawa 252-5258, Japan

<sup>4</sup> Department of Applied Physics, Faculty of Engineering, University of Miyazaki, 1-1 Gakuen Kibana-dai Nishi, Miyazaki, 889-2192, Japan

<sup>5</sup> Department of Physical Science, Hiroshima University, 1-3-1 Kagamiyama, Higashi-Hiroshima, Hiroshima 739-8526, Japan

<sup>6</sup> Department of Physics, The University of Tokyo, 7-3-1 Hongo, Bunkyo-ku, Tokyo 113-0033

(TK): kouzu@heal.phy.saitama-u.ac.jp

(Received ; accepted )

## Abstract

The Crab Nebula is one of the brightest and most stable sources in the X-ray sky. Year-scale flux variation from the object was recently revealed in the hard X-ray band by four satellites. This marked the first detection of year-scale variability from pulsar wind nebulae in the hard X-ray band. The Crab Nebula has been observed at least once a year for calibration purposes with the Suzaku Hard X-ray Detector (HXD) since its launch in 2005. In order to investigate possible spectral changes as well as flux variation, the archival data of the HXD were analyzed. The flux variation reported by other instruments was confirmed in the 25 – 100 keV band by the HXD in a few percent level, but flux above 100 keV did not follow the trend in variation below 100 keV. The hardness ratios produced utilizing the PIN and GSO sensors installed in the HXD exhibit significant scattering, thereby indicating spectral variations in the hard X-ray. The spectral changes are quantified by spectral fitting with a broken power-law model. The difference between the two photon indexes of the broken power-law model in harder and softer energy bands is in the range of  $< 2.54$ . Taking into account flux variation of 6.3% and spectral variation time-scale of a few days, multi components of the broken power-law-shaped synchrotron emission with different cooling times are suggested.

**Key words:** radiation mechanisms: non-thermal — ISM: individual (Crab Nebula) — pulsars: individual (PSR B0531+21) — X-rays: stars

## 1. Introduction

The Crab Nebula is one of the most famous pulsar wind nebulae (PWNe) which is located in the center of a historical supernova first recorded in Japan and China in 1054 (Duyvendak 1942). An energetic, bright pulsar (known as Crab pulsar=PSR B0531+21) exists in the center of the Crab Nebula. The Crab Nebula has been observed in the entire observable electromagnetic wavelength from radio to TeV gamma-rays. From the non-thermal spectrum and strong polarization (Weisskopf et al. 1976; Forot et al. 2008), emissions from the object are interpreted as synchrotron radiation in the X-ray band. Emissions from the direction of the object are divided into PWN and pulsar components. These two components can be separated not only by imaging analyses but also by phase-resolved timing analyses if we assume the emission from the pulsar is almost the same as the pulsed emission. Therefore, they are separately observed and discussed by many authors even in the hard X-ray band, where it is hard to get im-

ages. The flux of the pulsar component accounts for  $\sim 20\%$  of the total flux with most of the rest stemming from the PWN in the hard X-ray band.

The pulsar essentially drives the electromagnetic radiation as follows: energetic flows of electrons and positrons from the pulsar (pulsar winds) reach and interact with interstellar mediums to induce a termination shock. The high energy particles are believed to radiate synchrotron emission outside of the shock. This radiation is called as PWNe. Since the origins of the emissions of pulsars and PWNe are the rotation of magnetosphere of the neutron star, they had been believed to be stable in principle.

Data stored in  $\sim 12$  years recently indicated 10 percent flux variation in 10 – 300 keV with hard X-ray instruments (Wilson-Hodge et al. 2011). As reported by Wilson-Hodge et al. (2011), the pulsed flux of the Crab pulsar in the 2 – 100 keV band slightly decreased by  $0.2\% \text{ yr}^{-1}$ , which is negligible for hard X-ray variation. Therefore the variation seen in the Crab observations is supposed to be due to that of the flux of PWN. Currently, there are no rea-

sonable models to account for the variation of the flux of PWN. Wilson-Hodge et al. (2011) also suggest the softening phenomena in the light curves of  $< 100$  keV with Fermi/GBM and INTEGRAL/ISGRI.

As indicated by Jourdain & Roques (2009) and Ling & Wheaton (2003), the X-ray spectrum from the Crab Nebula is described by the broken power-law model, whose break energy is at about 100 keV. This break can be explained by electron cooling via synchrotron radiation. Thus the break point and the index may be changed in accordance to the flux change. In fact, Ling & Wheaton (2003) reported variable broken power-law spectra with CGRO/BATSE, while Jourdain & Roques (2009) could not confirm the phenomenon. Thus, the existence of the variation in the broken power law spectrum was unclear. Here we analyzed the archival data of the Crab Nebula obtained by the Suzaku Hard X-ray Detector (HXD), which offers the best sensitivity in the range of 10 – 600 keV.

Since the promising variability could be so small compared with the systematic errors in the standard calibration of the instruments, in principle, we have to clarify the validity of the energy response matrix including the effective area before the spectral analyses. This paper reports on spectral variations with close attention paid to instrumental calibration, and is organized as follows: Section 2 discusses the observations and the method of data reduction employed. Section 3 describes the results obtained. In Section 3.2, we first examined the spectral changes without model fittings in order to reduce possible errors from the uncertainty of the response matrices and the method of model fittings. Then in Sections 3.3 to 3.5, we performed model fittings to the spectra in order to quantitate the spectral changes. Section 4 describes the analysis and results regarding the pulsar component. Finally, Section 5 discusses the origin of the observed variability.

## 2. Observation and Data Reduction

### 2.1. Observation

We used data observed by the PIN (10 – 70 keV) and GSO ( $\text{Gd}_2\text{SiO}_5(\text{Ce})$ ; 40 – 600 keV) of the HXD (Takahashi et al. 2007; Kokubun et al. 2007) on board Suzaku (Mitsuda et al. 2007). The HXD has two advantages in investigating hard X-ray spectral variability: wide-band sensitivity in 10 – 600 keV, and small background rate and high reproducibility (i.e., smaller systematic errors) of the background model. Suzaku also carries CCDs called the X-ray Imaging Spectrometer (XIS; Koyama et al. 2007). However these devices are difficult to use for this study due to a pileup problem when observing the bright object like the Crab Nebula. For this reason, we did not use the XIS data in this work.

There are two typical observation attitudes for Suzaku corresponding to the optical axes of the XIS and HXD (respectively called “XIS nominal” and “HXD nominal”). Suzaku observed the Crab Nebula with both nominal positions to check the effective areas and energy responses. Observations for this purpose were made 17 times from

July 2005 to March 2012, and all data were public soon after the observations. In order to avoid relative large uncertainty in calibration, we excluded the datasets other than nominal pointing positions; i.e., offset observations of the Crab Nebula, which is used to define the optical axes at the initial phase of the satellite.

The effective area of the HXD is different by the nominal positions simply due to the transparency of its fine collimator. Takahashi et al. (2007) and Kokubun et al. (2007) show that the ratio between effective areas of the HXD and XIS nominal positions is about 92%, and the differences in energy dependencies of the effective area between them is within 1% in 15 – 70 keV and 2% in 50 – 600 keV. Every response matrix is defined for a period, “epoch”, which is divided by the change of operational parameters; combination of a bias voltage and a set of lower discriminator (LD) level. Table 3 of Nishino et al. (2010) summarizes the history of these operations.

### 2.2. Data Reduction

The gain changes of the PIN are within 1% (Nishino et al. 2010). We also confirmed the PIN gain stability with accuracy of  $< 0.7\%$  until 2012 September after the study by Nishino et al (2010), by measuring the Gd K lines produced in GSO crystals which are irradiated by X-rays from objects (Kouzu 2013). The gain of the photomultipliers for GSO changes in various timescales, so that the GSO gain history files are constantly revised along with calibration results. The energy scale in  $< 100$  keV was also improved by the FTOOLS `hxdpi` (Yamada et al. 2011). All HXD data were reprocessed with `aepipeline` version 1.0.1 in the HEADAS 6.11 software package using CALDB 2011-09-15; therefore, the GSO data were applied to `hxdpi` version 2010-01-12 and the gain history `gsogpt` in this work.

Background for the HXD data is generated as a synthetic model that accounts for the time-variable particle background (the “non X-ray background”, NXB; Fukazawa et al. 2009). Specifically, we used the “tuned” PIN NXB models of version 2.0 (METHOD=LCFITDT, METHODV=2.0pin0804). We also used the GSO NXB models of version 2.5 (METHOD=LCFIT, METHODV=2.5ver0912-64) for observations before November 2011, and those of version 2.6 (METHOD=LCFIT, METHODV=2.6ver1110-64) after November 2011. The uncertainty of the NXB models of the PIN is within 3% (Fukazawa et al. 2009), which is negligible as the Crab source count rate is 10 times greater than that of NXB, even if at 70 keV. The uncertainty of the GSO NXB is less than 1% (Fukazawa et al. 2009).

In the estimation of the flux from the object, it is important to calculate the dead time (or live time) of the observation. The dead time of the HXD-PIN and GSO is calculated regarding the following three processes: (1) event processing stopped by another process running previously triggered, (2) an event data packet discarded in communication between the HXD analog electronics and digital electronics, and (3) space packets containing events discarded due to limited bandpass between the digital elec-

tronics and data processor. In particular, the HXD team tunes the parameters of analog electronics, and so the case (2) only occurs just after South Atlantic Anomaly passages. Also, we discard events during the periods in case (3) by the FTOOL `hxdgtigen`. The dead time is calculated and stored with the pulse height data obtained by the FTOOL `hxddtcor`. The dead time fraction is determined with accuracy of  $< 0.2\%$  at an observation duration of  $> 10$  ks (Kokubun et al. 2007).

### 3. Analysis of Total Emission

#### 3.1. Flux Variation

In order to examine the time variation of total flux (pulsar + nebula) reducing effects by any systematic uncertainty of the instrumental responses, we evaluate the count rates of individual observations by subtracting both the non X-ray background and cosmic X-ray background from events. We also have to note that different bias voltages for PIN were applied during epoch 1, epoch 2 and after epoch 3, as represented in Table 3 of Nishino et al. (2010). Effective areas for each epoch is calculated based on ground tests (Sugiho et al. 2001; Nishino et al. 2010). In order to compare the measured flux in each epoch, here we normalized the photon flux using the calculated effective area for each epoch. In addition to the effect of bias voltage, the effective area decreases at  $< 25$  keV because of LD of each PIN detector. Besides, the detector's responses above 55 keV were affected by the degraded depth of depletion layers, which is adjusted by using the calibration data-sets on the Crab Nebula itself. Therefore, we only used the 25 – 55 keV band where the effective area of the response matrices changes within 1% for observations after PIN epoch 3. Responses of this energy band depend on neither signal processing nor time degradation, and are only defined simply by the physical process; cross section of the photo absorption process, or a stopping power of Si of the PIN diode (Nishino et al. 2010; Kokubun et al. 2007). The count rates are normalized by the effective area calculated for each observation, taking into account the difference in effective area according to different nominal positions.

Figure 1 shows the variation of total count rates with the HXD and other X-ray detectors normalized with the count rates in MJD 55000 – 55500. The count rates in 25 – 55 keV and that in 50 – 100 keV are consistent with the year-scale trends by other satellites except for the data after MJD 55500. On the other hand, the trend of the GSO data in 100 – 500 keV deviates from trends of the other energy bands even when the data include statistical errors ( $1\sigma$ ) and systematic errors (1% of the NXB). In addition to the year-scale changes, a day-scale variation of  $\sim 1\%$  with the PIN and GSO is also represented, which is derived from a ratio between count rates of 2006.03.30 and 2006.04.04 whose configurations (PIN epochs and nominal positions) are the same (see Table 1 for the time intervals and count rates).

#### 3.2. Hardness Ratios

To clarify the year-scale and day-scale variations (Section 3.1) without model fittings, we produced the hardness ratios of the PIN and GSO datasets. Figure 2 shows the count rates vs. hardness ratios of the PIN and GSO. The count rates (horizontal axes) are normalized by the effective area calculated for each observation, taking into account for different nominal positions. To avoid mixing the data of different detectors (i.e, different energy response matrices), here we plotted hardness ratios of the PIN and GSO individually. When observing such bright sources as the Crab Nebula, Gd K lines ( $\sim 43$  keV) from the GSO had not been reproduced with sufficient accuracy in the response (Nishino et al. 2010). We did not use the energy range of 40 – 45 keV to avoid the Gd K line structure.

In order to check correlations between hardness ratios and count rates, we fitted the data with linear functions, and then got  $\chi^2/\text{d.o.f} = 16.72/10$  (PIN) and  $47.96/15$  (GSO). Hypotheses of linear correlations are rejected on 91.9% (PIN) and  $> 99.9\%$  (GSO) confidence levels. In other words, both the hardness ratios and individual count rates vary significantly, but neither shows any unique correlation. Moreover, the hardness ratios of the soft band and hard band behave differently, suggesting a variable break energy or photon indexes in spectra which they are described by the broken power law model, as indicated by Ling & Wheaton (2003).

#### 3.3. Individual Spectra

The level of the observed variation ( $\sim 6.3\%$ ) of PIN 25 – 55 keV count rates, as evaluated in section 3.1, is fairly close to the sum of official values of the systematic errors of released response matrices (gain stability), NXB, and dead time correction ( $< 1.2\%$  total at  $< 100$  keV; Section 2.2). Here we summarize evidences showing that the above analysis is reliable. As the response matrices of the HXD-PIN (25 – 55 keV) and GSO are constructed only in line with Geant4 simulations with parameters obtained in ground tests (Terada et al. 2005), they have not been tuned or calibrated with the Crab Nebula. Thus we reasonably consider the response matrices to be independent of the flux variation of the Crab Nebula. As mentioned in Section 3.1, the HXD flux trend was consistent with other satellites at  $3\pm 1\%$  (PIN 25 – 55 keV),  $1\pm 1\%$  (GSO 50 – 100 keV), and  $4\pm 1\%$  (GSO 100 – 500 keV), taking into account day-scale variability as the second errors (Fig. 1). These facts support the conclusions that effective areas of the PIN 25 – 55 keV, GSO 50 – 100 keV and 100 – 500 keV are essentially stable within 4%, 2% and 5% at most respectively, and that the relative flux variation is real.

Before evaluating individual spectra, we first performed a model fitting of the averaged spectrum of all HXD observations in 25 – 40, 45 – 55 keV as a template to evaluate spectral variations, using the averaged response matrix weighted by individual exposures. We used a single power-law model in order to see possible spectral break in



comparison with the simple model. The values of the photon index and flux are  $2.141 \pm 0.006$  and  $9.65^{+0.1}_{-0.2} \times 10^{-9}$  erg cm $^{-2}$  s $^{-1}$  (25 – 55 keV) at a 90% confidence level with the  $\chi^2/\text{d.o.f.} = 68.54/63$ .

Second, we compared individual spectra with this model. We used the appropriate arf files (`ae_hxd_gsohxnomb_crab_20100526.arf` or `ae_hxd_gsoxinomb_crab_20100526.arf`) for all the GSO spectra, in addition to the response matrices (`ae_hxd_gsohxnomb_20100524.rsp` or `ae_hxd_gsoxinomb_20100524.rsp`) for the aiming positions (HXD nominal and XIS nominal). The GSO arfs are empirical functions to correct the normalization of the GSO for matching that of the PIN, implemented as spline functions converging to a constant above 100 keV (Yamada et al. 2011), and the reference therein<sup>1</sup>. Figure 3 shows the ratios of individual spectra to the averaged best-fit power-law model. This figure clearly demonstrates the variations of the spectral break at  $\sim 100$  – 200 keV. For instance, the spectral slope was steep in the spectra of 2005.09.15, 2008.08.27, and 2012.03.14/26, while flat in the spectra of 2007.03.20 and 2009 – 2010.

### 3.4. Quantitative Analysis of the Averaged Spectrum

The hard X-ray spectrum (around  $\sim 100$  keV) of the Crab Nebula is well represented by a broken power-law model (e.g., Yamada et al. 2011), although Jourdain & Roques (2009) reported that a log parabolic law (Massaro et al. 2000; Massaro et al. 2004) is better fitted with the spectrum rather than a broken power law. We thus tested several models for the hard X-ray spectrum using the HXD data. We averaged all spectra of the observations listed in Table 1. We performed fittings with a single power law

$$A(E) = KE^\Gamma, \quad (1)$$

an exponential cutoff power law, a log parabolic law<sup>2</sup>, the Band function (Band et al. 1993), and a broken power-law model

$$A(E) = KE^{\Gamma_1} (E < E_{\text{break}}), \quad (2)$$

$$= KE_{\text{break}}^{\Gamma_1 - \Gamma_2} \left( \frac{E}{1 \text{ keV}} \right)^{\Gamma_2} (E \geq E_{\text{break}}) \quad (3)$$

to the averaged spectrum. We adopted the average responses calculated according to the exposure time of each observation mode (attitude and PIN epoch). Here we note that the spatial extension of the Crab Nebula ( $\sim 1$  arcmin in diameter in hard X-ray band; Pelling et al. 1987) can be negligible due to the HXD angular response whose field of view is  $34' \times 34'$  ( $< 100$  keV) and  $4.5^\circ \times 4.5^\circ$  ( $> 100$  keV) (FWHM) exhibit flat top effective areas within  $\sim 2$  arcmin in diameter.

Figure 4 shows the averaged spectrum and ratio of the spectrum to the best-fit models. Table 2 lists the best-fit parameters. The single power-law model shows large

residuals at  $> 100$  keV to imply that a cutoff or break is necessary in this energy band. Although the model of the second smallest  $\chi^2/\text{d.o.f}$  is the cutoff power-law model, the best-fit cutoff energy is much larger than the energy band of the HXD data. The broken power-law model, which is an empirical model for the Crab hard X-ray spectrum, succeeded to represent the data with the smallest  $\chi^2$  among the five models above 100 keV range. We still see a residual structure in 25 – 55 keV band. This may suggest spectral variation in the observations.

### 3.5. Quantitative Analysis of Individual Spectra

In order to evaluate the spectral variation quantitatively, we performed model fittings for individual spectra with the broken power-law models, which provides the smallest  $\chi^2$  for the averaged spectrum (Section 3.4). As shown in Figure 5 and Table 3, all the spectra are reproduced by the broken power law model and we also note that the residual structure seen in the averaged spectra is disappeared in these time resolved spectra. Figure 6 shows the distribution of derived  $\Gamma_1$  and  $\Gamma_2$ , which are photon indexes below and above the break energy, respectively. Figure 7 represents the derived break energy ( $E_{\text{break}}$ ) from each observation. In Figure 6 and Figure 7, we evaluate the errors of the best fit values including systematic errors due to the reproducibility of the GSO NXB, by varying the derived NXB models by  $\pm 1\%$ . Hypotheses that  $\Gamma_1$ ,  $E_{\text{break}}$  and  $\Gamma_2$  were constant are safely rejected at  $> 99.9\%$ ,  $99.7\%$  and  $91.7\%$  confidence levels, respectively, taking into account both statistic and systematic errors. The very conservative upper limit of  $\Gamma_1 - \Gamma_2$  is 2.54 considering the upper limit of  $\Gamma_1$  and the lower limit of  $\Gamma_2$  at the 90% confidence range. The upper limit of  $\Gamma_1 - \Gamma_2$  will be reduced  $< 1.29$  if we exclude the data point at 2006.03.30, whose  $\Gamma_1 - \Gamma_2$  is exceptionally large, 2.54, mainly because the value of  $\Gamma_1$  allows  $\Gamma_1 = 0$ . We fitted  $\Gamma_1 - \Gamma_2$  with a constant as a function of MJD, and found that the best-fit constant value is  $0.16 \pm 0.02$  at a  $1\sigma$  error with  $\chi^2/\text{d.o.f.} = 23.74/16$ . In Fig. 6 and Table 3, the errors increase by time because the level of NXB is increased due to accumulated events from radio active nuclei by cosmic-rays in GSO crystals.

We also examined an exponential cutoff power-law model for the spectrum. Figure 8 shows the best-fit photon indexes and cutoff energies ( $E_{\text{cut}}$ ). We cannot obtain conclusive results with this model, as all best-fit values for  $E_{\text{cut}}$  fairly exceed the energy range of the HXD data (500 keV).

## 4. Analysis of the Pulsed Component

### 4.1. Pulse Profiles

To understand how the pulsed component of the pulsar affects the variation of total emission from the Crab Nebula, we investigated the fluctuations of pulse profiles and pulsed flux of the Crab pulsar.

We adopted the pulse period ( $P$ ) and its time-derivative ( $\dot{P}$ ) from the Jodrell Bank Crab Pulsar Monthly

<sup>1</sup> [http://heasarc.gsfc.nasa.gov/docs/suzaku/analysis/gso\\_newarf.html](http://heasarc.gsfc.nasa.gov/docs/suzaku/analysis/gso_newarf.html)

<sup>2</sup> We installed and used the `logpar` model as downloaded from <http://heasarc.gsfc.nasa.gov/xanadu/xspec/models/logpar.html>

Ephemeris<sup>3</sup>. Epoch (phase=0) was defined as the arrival time of the first peak in the radio band. We used *aebarycen* (Terada et al. 2008) to correct photon arrival times at UTC in orbit to those at the solar system barycenter, assuming that the Crab pulsar is located in the position of R.A. =  $5^{\text{h}}34^{\text{m}}31^{\text{s}}.97232$ , Decl. =  $+22^{\circ}00'52''.0690$  (J2000), on which is the same coordinate used by the Jodrell Bank Crab Pulsar Monthly Ephemeris.

Figure 9 shows the pulse profiles observed with the HXD at the HXD nominal pointing position shown in count  $\text{s}^{-1}$ . Here, we defined On and Off phases at phase 0.9 – 1.5 and 0.55 – 0.85, respectively. The averaged counts at the Off phase are subtracted in the plot. The relative intensity of the first pulse peak with respect to the second one increases with the energy. The X-ray pulse peak leads to the first radio pulse peak (phase = 1 in Fig.9) by  $\sim 300 \mu\text{s}$ , which is consistent with results previously reported by other satellites (Rots et al. 2004; Kuiper et al. 2003) and the initial observations with the HXD (Terada et al. 2008). The pulse profiles were consistent with each other within  $2.7\sigma$  of statistical errors of each phase bin through all observations in 25 – 300 keV.

#### 4.2. Pulsed Flux

We searched for variations of the pulsed flux using all data at both nominal pointing positions. Count rates of the pulsed components, “On–Off” are plotted in Figure 10. Numerically, the best fit values in fitting of data in Figure 10 with a constant model are  $1.68 \pm 0.01 \text{ count s}^{-1}$  and  $\chi^2/\text{d.o.f.} = 23.03/16$  at PIN 25 – 40, 45 – 55 keV,  $6.42 \pm 0.04 \text{ count s}^{-1}$  and  $\chi^2/\text{d.o.f.} = 38.96/16$  at GSO 50 – 300 keV with the errors at 90% confidence level. Hypotheses for the constants are rejected at 88% and 99% confidence levels, respectively. The pulsed component contributes only about 20% of the total flux, and thus, the possible  $\sim 1\%$  of variations are hard to account for the total variation of the hard X-rays shown in Fig. 1 with the fluctuation of the pulsed component.

### 5. Discussion

In Section 3.1, we demonstrated the long-term photon flux variation measured by the HXD, which is consistent with those measured by other X-ray satellites within 3 – 4% (see also Section 3.3). The relative peak-to-peak amplitude of the flux variation was 6.3% in 25 – 55 keV. As indicated in the hardness ratio (Section 3.2), we evaluated the spectral variation quantitatively (Section 3.5) to find that the difference between the photon indexes below and above the break energy varies. Because the flux of the pulsed component contribute only  $\sim 20\%$  of the total flux (Section 4), the variation seen in the total flux may be caused by the nebular component (the Crab Nebula). The following sections discuss the origin of the variation of X-ray fluxes and energy spectra.

#### 5.1. Comparison with Previous Works

Our results obtained by the Suzaku HXD confirmed year-scale flux variation reported by Wilson-Hodge et al. (2011) using RXTE, INTEGRAL, Swift and Fermi. They also claimed softening in MJD 54690 – 55390 in flux decreasing at  $<100 \text{ keV}$ . Our results agree with their arguments regarding the general trend during this time interval, although the HXD results do not show simple softening in detail (Fig. 2). In the range of 100 – 300 keV, they reported less decrease than in the softer band in MJD 54690 – 55390 with INTEGRAL/ISGRI. We observed similar phenomena in the HXD data, which showed less flux variation in the 100 – 500 keV than those of the 25 – 55 and 50 – 100 keV bands. However, the PIN count rate seems to exhibit slightly larger values than those of other instruments after MJD 55500 by about 3 % (Fig. 1). This may be due to secular degradation of charge transfer efficiency in PIN detector. In order to examine the possibility, we checked the PIN gains using Gd K line from GSO crystal and found the PIN gains in this duration might be reduced by  $-0.5 \pm 0.7 \%$ . Assuming the Crab spectrum this corresponds to the tolerance of  $-1.7^{+3.4}_{-2.5} \%$  in the photon flux, which can explain the apparent discrepancy. But we stress that a hypothesis that  $\Gamma_1$  values were constant is rejected at a  $> 99\%$  confidence level, even if we omit the data after MJD 55500 during which the PIN gain might have been degraded.

#### 5.2. Origin of the Variable Component

The X-ray radiation of the Crab Nebula is generally regarded as synchrotron radiation because of the non-thermal spectrum and the strong polarization. From our analysis, the averaged hard X-ray spectrum is represented by the broken power-law model with  $E_{\text{break}} \sim 100 \text{ keV}$  (Section 3.4). In the PWN, electrons are re-accelerated and continuously injected from the termination shock, and then cooled down via synchrotron radiation. Assumed synchrotron radiation, the higher energy electrons are cooled in the shorter cooling time ( $\tau_c$ ). According to the nomenclature of Sari et al. (1998), when  $\tau_c$  of the minimum Lorentz factor electrons is shorter than a duration ( $t_0$ ) for each spectrum radiation, which presumably corresponds to the electron passage time through the emission region, the regime is called “fast cooling” regime. If it is the case of “fast cooling”, the observed  $E_{\text{break}}$  corresponds to either of  $\nu_a$ ,  $\nu_c$  or  $\nu_m$ , and the observed  $\Gamma_1$  is either 1,  $-2/3$ , or  $-3/2$ . However, none of those values are accepted by any of the measured  $\Gamma_1$  except for 2006.03.30 (Table 3), meaning the observed spectra reject the “fast cooling” regime. We note that  $\Gamma_1$  of 2006.03.30 has a large error as  $E_{\text{break}}$  cannot be well derived. On the other hand, in the case of the “slow cooling” regime ( $t_0 < \tau_c$ ),  $\Gamma_1$  should be either 1,  $-2/3$ , or  $-(p+1)/2$ , and  $E_{\text{break}} = \nu_a$ ,  $\nu_m$ , or  $\nu_c$ , respectively. The observed values of  $\Gamma_1$  accept only the case of  $E_{\text{break}} = \nu_c$  in the “slow cooling” regime.

Although  $\Delta\Gamma = \Gamma_1 - \Gamma_2$  should be 0.5 in the slow cooling regime since  $\Gamma_2$  should be  $-(p+2)/2$ , 14 out of 17 data of ours would not accept the expected value assum-

<sup>3</sup> <http://www.jb.man.ac.uk/~pulsar/crab.html>

ing a simple one-zone model ( $\Delta\Gamma = 0.5$ ). However here we have to notice that significant spatial and temporal variations are reported in the soft X-ray band (Greiveldinger & Aschenbach 1999; Hester et al. 2002; Mori et al. 2004a), which naturally implies multicomponent variable spectra also in the hard X-ray band. Moreover the filamentary structures seen in the Chandra images (Hester et al. 2002; Mori et al. 2004b) suggest that magnetic fields are different by locations in the Crab Nebula. On the other hand, the photon indexes of X-ray spectra are about 2 anywhere in the Crab Nebula (Mori et al. 2004b), energy spectra of re-accelerated electrons are thought to have almost constant indexes. Considering these facts, the multicomponent spectra are observed as an ensemble of power-law components and broken power-law components (with  $\Delta\Gamma = 0.5$ ) in the limited observed energy band. Consequently, we observe variable broken power-law spectra with  $0 < \Delta\Gamma < 0.5$  as superpositions of these components in the energy band. In fact, all of our data accept the expected range of  $0 < \Delta\Gamma < 0.5$ .

Magnetic field strength  $B$  related to synchrotron radiation is given as:

$$\frac{B}{100 \mu\text{G}} \sim \left( \frac{\tau_c}{1 \text{ year}} \right)^{-2/3} \left( \frac{E_{ph}}{100 \text{ keV}} \right)^{-1/3} \quad (4)$$

where  $E_{ph}$  is the photon energy. The synchrotron bolometric intensity ( $P \propto B^2 n(\gamma) \gamma^2$ ) is assumed to be proportional to the hard X-ray flux, where  $n(\gamma)$  is the electron number density as a function of the Lorentz factor of electron  $\gamma$ . In the slow cooling regime,  $\tau_c$  should be comparable with the timescale of passages of electrons that are pertinent to  $\nu_c$ . From our results, the timescale of the flux variation is expected to be a few days (Section 3.1). By adopting a timescale of five days, for example, we can estimate the value of  $B$  to be  $\sim 1.7$  mG from Equation 4. Because the cooling timescale can be regarded as the passage time scale, the typical scale of the variable emission region is estimated to be around  $0.35 - 1.25$  light-days ( $\sim (3.2 - 8.1) \times 10^{-4}$  pc), under the assumption of the speed of plasma in the PWN measured with Chandra ( $0.07 - 0.25c$ ; Mori et al. 2004b). Although the scale of the variable region is  $\sim 0.1\%$  of the whole X-ray emission region, the mismatch between the occupancy (about  $0.1\%$  of the whole X-ray emitting region) and the factor of the flux variations ( $8\%$  of total flux) can be solved when the variable region has  $\sim 10$  times higher magnetic field strength than those in others, because  $P \propto B^2$  as mentioned before. Of course, because  $P$  has a dependency with  $n(\gamma)$  or  $\gamma$ , we may assume that a multiple component has a different density or Lorentz factor, but we do not discuss these possibilities here due to limitation of information which we have currently. We must wait for hard X-ray images to conclude the entire morphology of the variable emission region and the magnetic fields.

We would like to acknowledge Takayuki Yuasa, Shinpei Shibata and Yasuyuki Tanaka for their supports in analysis and discussion. We would like to thank the anonymous referee for the valuable comments and suggestions, which

significantly improved our paper. We wish to thank all members of the Suzaku operation team and the Suzaku HXD team. This research has made use of the MAXI data provided by RIKEN, JAXA and the MAXI team. T.K is supported by the Grant-in-Aid for Research Fellowship for Young Scientists (DC2) of the Japan Society for the Promotion of Science (JSPS) No. 239311, and in part by the Grants-in-Aid for Scientific Research (B) from the Ministry of Education, Culture, Sports, Science and Technology (MEXT) (No. 23340055, Y.T; No. 22340039, M.S.T).

## References

- Atoyan, A. M., & Aharonian, F. A. 1996, MNRAS, 278, 525
- Band, D., Matteson, J., Ford, L., et al. 1993, ApJ, 413, 281
- Boldt, E. 1987, Observational Cosmology, 124, 611
- de Jager, O. C., Harding, A. K., Michelson, P. F., Nel, H. I., Nolan, P. L., Sreekumar, P., & Thompson, D. J. 1996, ApJ, 457, 253
- Duyvendak, J. J. L. 1942, PASP, 54, 91
- Forot, M., Laurent, P., Grenier, I. A., Gouiffès, C., & Lebrun, F. 2008, ApJL, 688, L29
- Fukazawa, Y., et al. 2009, PASJ, 61, 17
- Greiveldinger, C., & Aschenbach, B. 1999, ApJ, 510, 305
- Hester, J. J., et al. 2002, ApJL, 577, 49L
- Jourdain, E., & Roques, J. P. 2009, ApJ, 704, 17
- Jung, G. V., 1989, ApJ, 338, 972
- Kennel, C. F., & Coroniti, F. V., 1984, ApJ, 283, 710
- Kokubun, M., et al. 2007, PASJ, 59, 53
- Kouzu, 2013, Ph.D. Thesis, Saitama University
- Koyama, K., Tsunemi, H., Dotani, T., et al. 2007, PASJ, 59, 23
- Kuiper, L., Hermsen, W., Walter, R., & Foschini, L. 2003, A&A, 411, L31
- Ling, J. C., & Wheaton, W. A. 2003, ApJ, 598, 334
- Markwardt, C. B., Barthelmy, S. D., & Baumgartner, W. H. 2010, The Astronomer's Telegram, 2858, 1
- Massaro, E., Perri, M., Giommi, P., & Nesci, R. 2004, A&A, 413, 489
- Massaro, E., Cusumano, G., Litterio, M., & Mineo, T. 2000, A&A, 361, 695
- Matsuoka, M., Kawasaki, K., Ueno, S., et al. 2009, PASJ, 61, 999
- Meyer, M., Horns, D., & Zechlin, H.-S. 2010, A&A, 523, A2
- Mitsuda, K., et al. 2007, PASJ, 59, 1
- Mori, K., Burrows, D. N., Pavlov, G. G., et al. 2004a, Young Neutron Stars and Their Environments, 218, 181
- Mori, K., Burrows, D. N., Hester, J. J., et al. 2004b, ApJ, 609, 186
- Much, R., et al. 1995, A&A, 229, 435
- Nishino, S., et al. 2010, Proc. SPIE, 7732,
- Pelling, R. M., Paciesas, W. S., Peterson, L. E., et al. 1987, ApJ, 319, 416
- Rots, A. H., Jahoda, K., & Lyne, A. G. 2004, ApJL, 605, L129
- Sugih, M., et al. 2001, IEEE Trans. Nucl. Sci., 48, 426
- Sari, R., Piran, T., & Narayan, R. 1998, ApJL, 497, L17
- Takahashi, T., et al. 2007, PASJ, 59, 35
- Tashiro, M., Makishima, K., Ohashi, T., et al. 1995, PASJ, 47, 131
- Terada, Y., et al. 2005, IEEE Trans. Nucl. Sci., 52, 902
- Terada, Y., et al. 2008, PASJ, 60, 25
- Yamada, S. et al. 2011, PASJ, 63, 645

Weisskopf, M. C., Cohen, G. G., Kestenbaum, H. L., et al.

1976, ApJL, 208, L125

Wilson-Hodge, C. A., et al. 2011, ApJL, 727, L40

**Table 1.** Suzaku Observations of the Crab Nebula

Obs. ID	Date	MJD	Exposure*	Nominal position	PIN epoch	Count rate <sup>†</sup>
100023010	2005/09/15	53628	9.9 ksec	HXD	1	$7.141 \pm 0.028 \pm 0.003^{\S}$
100023020	2005/09/15	53628	12.4 ksec	XIS	1	$7.115 \pm 0.026 \pm 0.004^{\S}$
101004010	2006/03/30	53824	9.1 ksec	XIS	1	$7.162 \pm 0.030 \pm 0.004^{\S}$
101004020	2006/04/04	53829	12.5 ksec	XIS	1	$7.080 \pm 0.026 \pm 0.003^{\S}$
101003010	2006/04/05	52830	29.1 ksec	HXD	1	$6.965 \pm 0.016 \pm 0.003^{\S}$
101010010	2006/09/05	53983	18.3 ksec	XIS	2	$6.983 \pm 0.021 \pm 0.004^{\S}$
102019010	2007/03/20	54179	40.5 ksec	HXD	3	$6.733 \pm 0.013 \pm 0.003$
103007010	2008/08/27	54705	30.3 ksec	XIS	4	$7.040 \pm 0.016 \pm 0.003$
103008010	2008/09/01	54710	31.6 ksec	HXD	4	$6.966 \pm 0.015 \pm 0.003$
104001010	2009/04/02	54923	31.3 ksec	HXD	5	$6.888 \pm 0.015 \pm 0.003$
104001070	2010/02/23	55250	15.1 ksec	XIS	8	$6.795 \pm 0.022 \pm 0.004$
105002010	2010/04/05	55291	31.3 ksec	XIS	9	$6.794 \pm 0.016 \pm 0.004$
105029010	2011/03/21	55641	34.2 ksec	XIS	11 <sup>‡</sup>	$6.867 \pm 0.015 \pm 0.004$
106012010	2011/09/01	55805	33.9 ksec	XIS	11	$6.908 \pm 0.015 \pm 0.003$
106013010	2012/02/28	55986	34.0 ksec	XIS	11 <sup>‡</sup>	$6.876 \pm 0.015 \pm 0.003$
106014010	2012/03/14	56001	42.2 ksec	XIS	11 <sup>‡</sup>	$6.936 \pm 0.013 \pm 0.003$
106015010	2012/03/26	56012	22.9 ksec	XIS	11 <sup>‡</sup>	$6.961 \pm 0.018 \pm 0.003$
Total			437.7 ksec			

\* Dead time corrected exposure time.

<sup>†</sup> Count rate of the PIN in units of count s<sup>-1</sup> @ 25–55 keV. Errors are statistical and systematic errors of the NXB (3%) on 1 $\sigma$  levels. Each count rate of the XIS nominal is adjusted to the HXD nominal.

<sup>‡</sup> Unusual values of the PIN epoch are selected given the special PIN LD setting during observations.

<sup>§</sup> Count rates of Epoch 1 and 2 are normalized to Epoch 3.



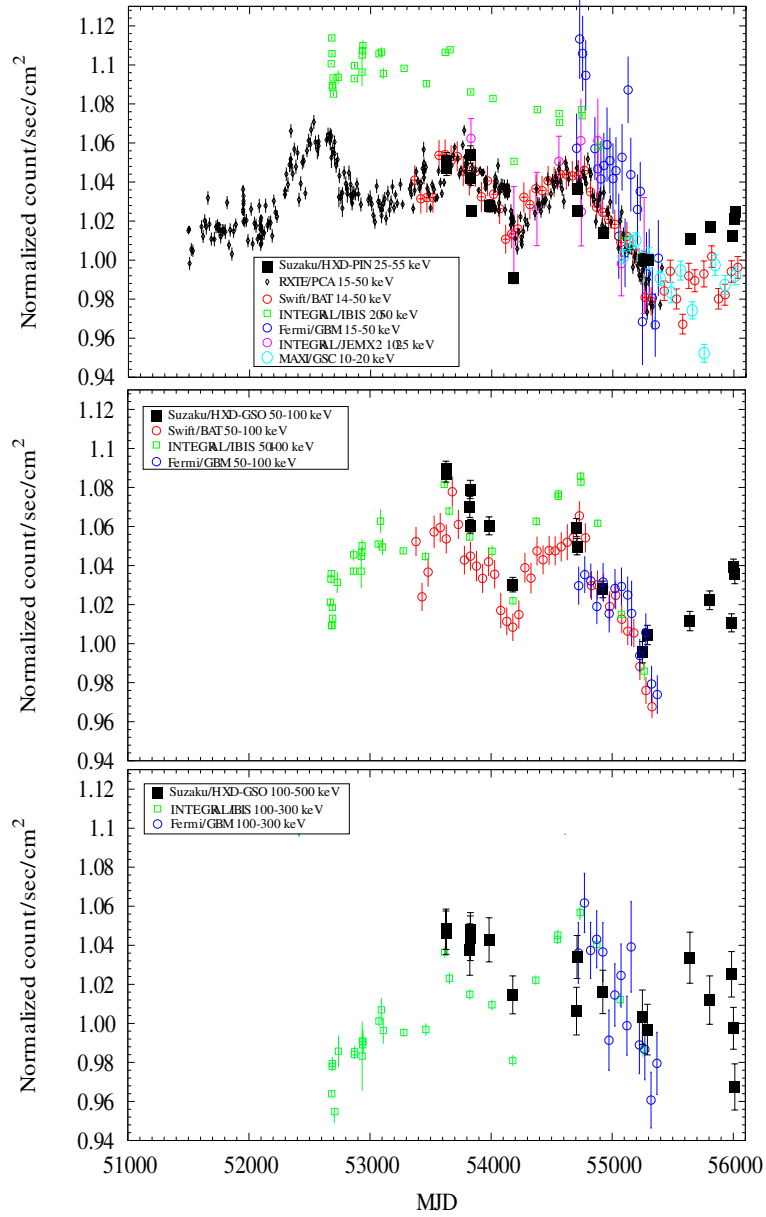


**Fig. 1.** Long-term light curves with the Suzaku/HXD in 25-55 keV (top), 50-100 keV (middle), and 100-500 keV (bottom) overlaid on data of Swift, RXTE, INTEGRAL, Fermi and MAXI. The data obtained by RXTE, Swift, INTEGRAL and Fermi before MJD 55000 are from Wilson-Hodge et al. (2011). Swift after MJD 55000 and MAXI (Matsuoka et al. 2009) are taken from their archival data [(Swift) <http://swift.gsfc.nasa.gov/docs/swift/results/transients/>, (MAXI) <http://maxi.riken.jp/>]. The error bars of the HXD include 1σ statistical errors and 1σ systematic errors of NXB (Fukazawa et al. 2009). Each flux is normalized to mean flux in the time interval of MJD 55000–55500.

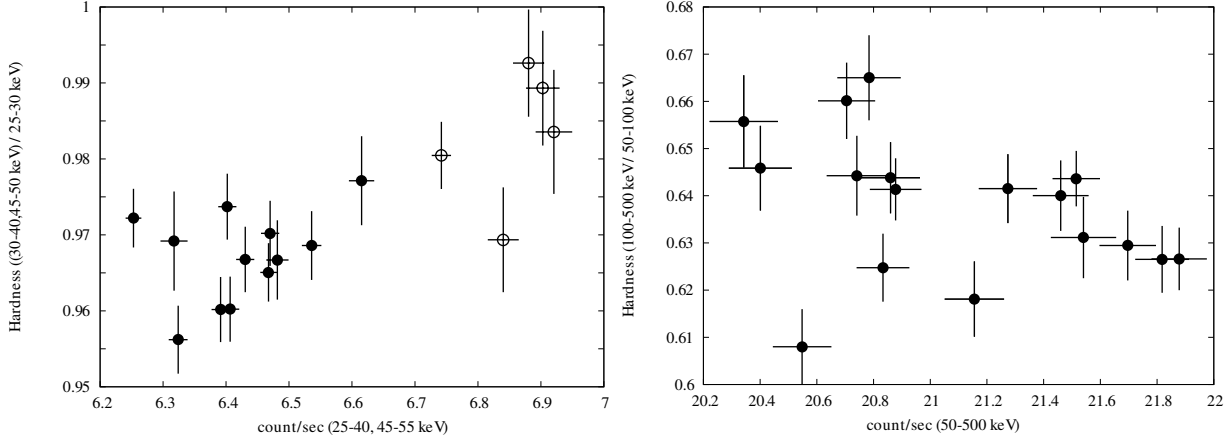


**Fig. 2.** Count rates vs. hardness ratios of PIN 30-40, 45-50 keV/25-30 keV (left) and GSO 100-500 keV/50-100 keV (right). The horizontal axes show count rates and the vertical axes show hardness ratios of count rates. Data marked with open circles in the left graph are only references because different bias voltages of the PIN were set in these observations. The error bars represent statistical errors ( $1\sigma$ ).

**Table 2.** Best-fit models of the averaged spectrum

Model name	Parameter name	Value (error)
Single power law	$\Gamma$	$-2.125 \pm 0.001$
	$\text{Flux}_s^*$	$0.970 \pm 0.009$
	$\text{Flux}_h^\dagger$	$7.865^{+0.008}_{-0.007}$
	$\chi^2 / \text{d.o.f.}$	$797.16 / 87$
Cutoff power law	$\Gamma$	$-2.075 \pm 0.004$
	$E_{\text{cut}}$ (keV)	$1396^{+134}_{-113}$
	$\text{Flux}_s^*$	$0.9728^{+0.0008}_{-0.0010}$
	$\text{Flux}_h^\dagger$	$7.951^{+0.008}_{-0.014}$
	$\chi^2 / \text{d.o.f.}$	$431.04 / 86$
Log parabolic law	$\alpha$	$-2.150 \pm 0.003$
	$\beta$	$-0.059 \pm 0.006$
	$_{\text{pivot}}E$ (keV)	20 (fix)
	$\text{Flux}_s^*$	$0.9739^{+0.0010}_{-0.0009}$
	$\text{Flux}_h^\dagger$	$7.948 \pm 0.011$
	$\chi^2 / \text{d.o.f.}$	$540.28 / 86$
Band function <sup>‡</sup>	$\alpha$	$-2.075^{+0.002}_{-0.004}$
	$\beta$	$> -2.387$
	$E_{\text{peak}}$ (keV)	$1378^{+542}_{-287}$
	$\chi^2 / \text{d.o.f.}$	$429.25 / 85$
Broken power law	$\Gamma_1$	$-2.115 \pm 0.002$
	$E_{\text{break}}$ (keV)	$134^{+7}_{-11}$
	$\Gamma_2$	$-2.26 \pm 0.02$
	$\text{Flux}_s^*$	$0.9700^{+0.0009}_{-0.0008}$
	$\text{Flux}_h^\dagger$	$7.916 \pm 0.009$
	$\chi^2 / \text{d.o.f.}$	$311.14 / 85$

All errors are presented at 90% confidence levels.

\* in units of  $\times 10^{-8} \text{ erg cm}^{-2} \text{ s}^{-1}$  at 25–55 keV

† in units of  $\times 10^{-9} \text{ erg cm}^{-2} \text{ s}^{-1}$  at 50–100 keV

‡ Flux of the Band function cannot be derived as  $\beta$  and  $E_{\text{peak}}$  have too large errors.

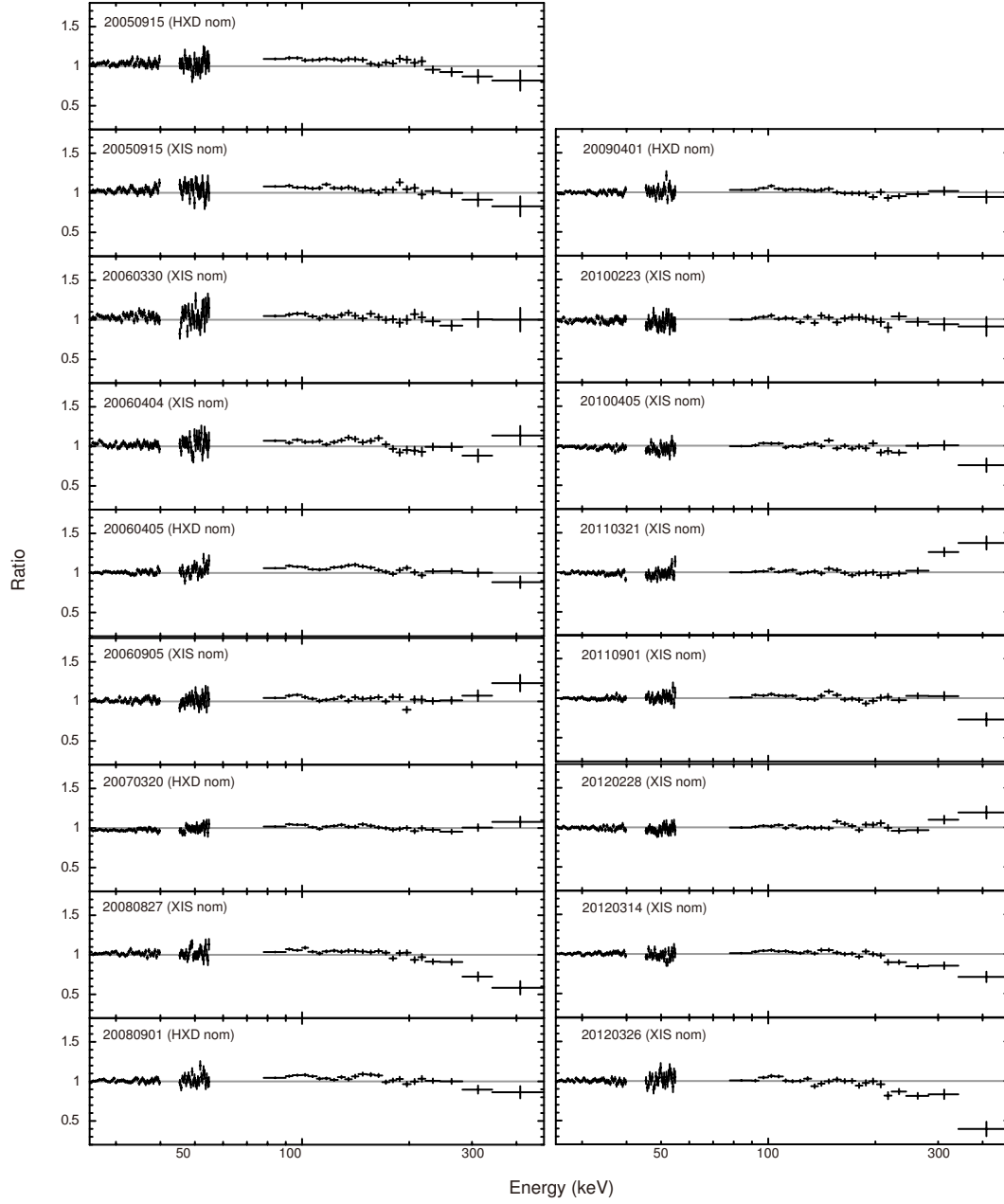


**Fig. 3.** Ratios of background-subtracted spectra of individual observations to the best-fit single power-law model of the averaged PIN spectrum (25-40, 45-55 keV) of all observations. The error bars represent statistical errors ( $1\sigma$ ).

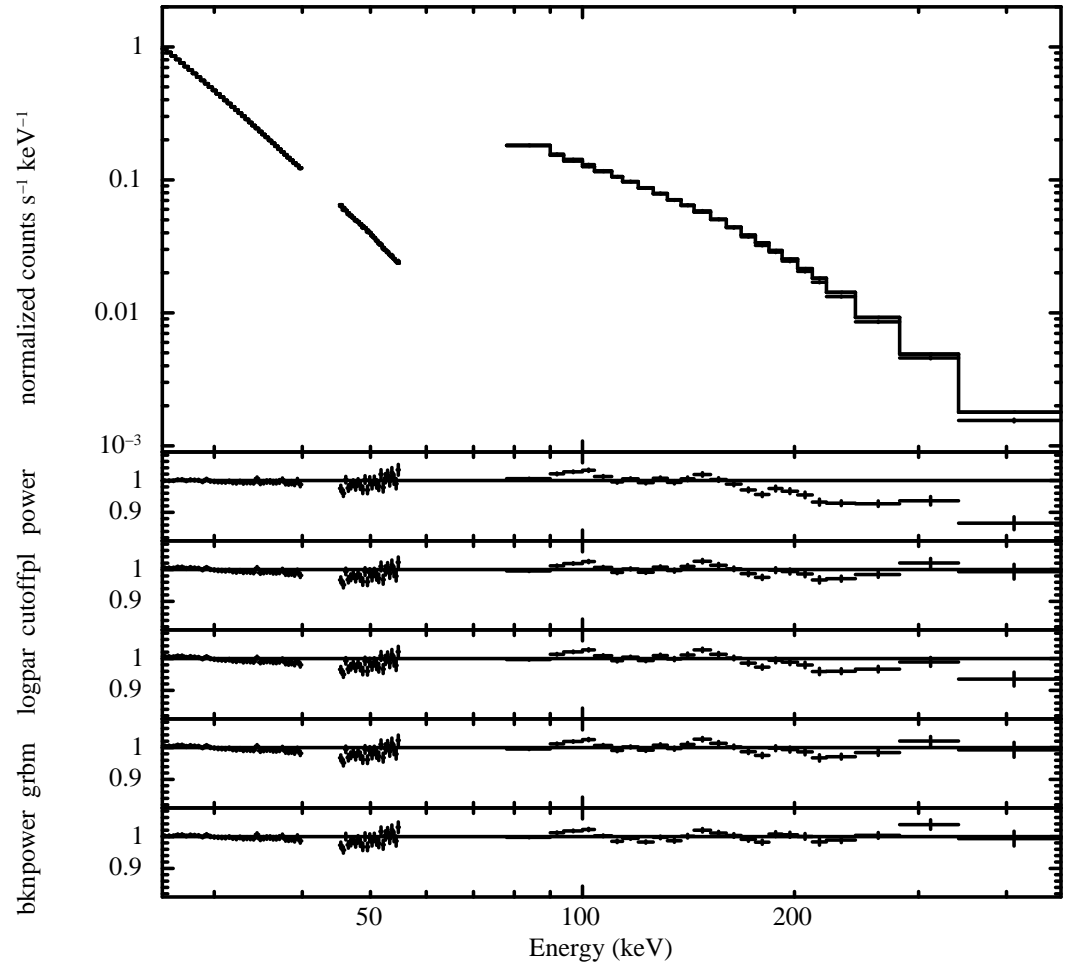


**Fig. 4.** The top panel shows the averaged spectrum through 2005–2012 with the Suzaku HXD. The solid line represents the best-fit single power-law model and crosses are data with  $1\sigma$  statistical errors. Below five panels show the ratios of the data to best-fit models of a single power law (power), an exponential-cutoff power law (cutoffpl), a log parabolic law (logpar), Band function (grbm), and a broken power law (bknpower).



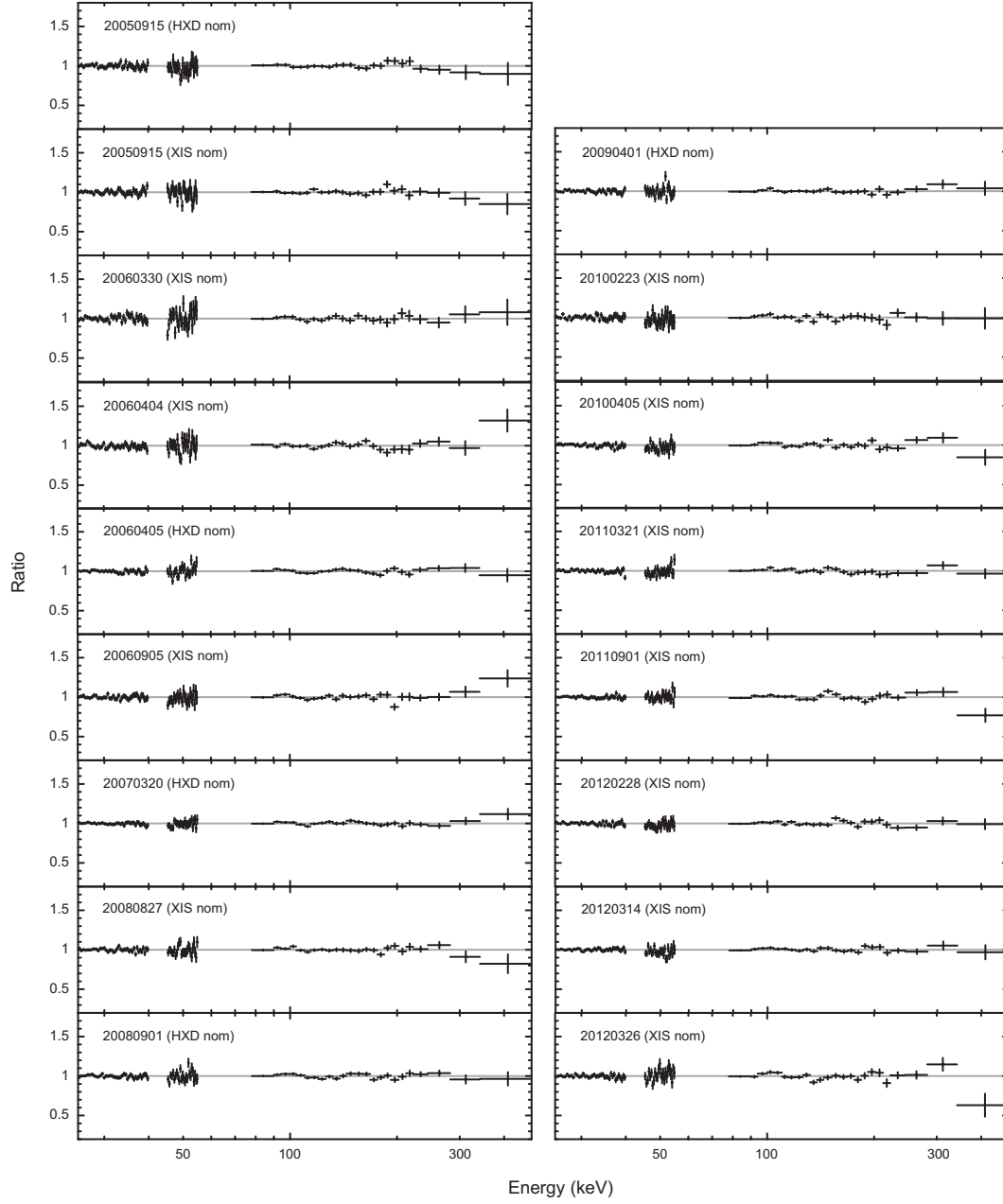


**Fig. 5.** Ratios of data to best-fit broken power-law models of individual spectra

**Table 3.** Best-fit broken power-law model of individual spectra

ObsID	Date	MJD	$\Gamma_1$	$E_{break}$ (keV)	$\Gamma_2$	Flux <sub>s</sub> *	Flux <sub>h</sub> †	$\chi^2$ ‡
100023010	2005/09/15	52628	$-2.093^{+0.014+0.007}_{-0.010-0.004}$	$120^{+22+5}_{-25-10}$	$-2.30^{+0.08+0.04}_{-0.10-0.10}$	$1.005^{+0.005}_{-0.006}$	$8.32^{+0.06}_{-0.06}$	63.86
100023020	2005/09/15	53628	$-2.093^{+0.020+0.004}_{-0.015-0.005}$	$92^{+29+8}_{-20-6}$	$-2.21^{+0.03+0.03}_{-0.06-0.08}$	$1.000^{+0.006}_{-0.006}$	$8.28^{+0.05}_{-0.1}$	78.39
101004010	2006/03/30	53824	$-2.125^{+0.018+2.107}_{-0.010-0.005}$	$132^{+38+29}_{-56-76}$	$-2.26^{+0.09+0.03}_{-0.14-0.14}$	$1.000^{+0.006}_{-0.006}$	$8.11^{+0.06}_{-0.07}$	88.45
101004020	2006/04/04	53829	$-2.109^{+0.008+0.000}_{-0.008-0.005}$	$141^{+16+1}_{-19-0}$	$-2.35^{+0.09+0.00}_{-0.11-0.12}$	$0.993^{+0.005}_{-0.005}$	$8.13^{+0.05}_{-0.05}$	109.82
101003010	2006/04/05	52830	$-2.094^{+0.005+0.011}_{-0.005-0.004}$	$135^{+12+1}_{-15-34}$	$-2.28^{+0.05+0.09}_{-0.06-0.09}$	$0.981^{+0.003}_{-0.003}$	$8.11^{+0.03}_{-0.03}$	122.97
101010010	2006/09/05	53983	$-2.106^{+0.012+0.000}_{-0.010-0.004}$	$92^{+17+304}_{-17-0}$	$-2.18^{+0.03+4.96}_{-0.03-0.05}$	$0.982^{+0.004}_{-0.005}$	$8.06^{+0.04}_{-0.10}$	96.36
102019010	2007/03/20	54179	$-2.093^{+0.007+0.003}_{-0.007-0.007}$	$99^{+20+12}_{-11-7}$	$-2.19^{+0.02+0.04}_{-0.03-0.10}$	$0.949^{+0.003}_{-0.003}$	$7.85^{+0.03}_{-0.05}$	85.28
103007010	2008/08/27	54705	$-2.120^{+0.006+0.008}_{-0.006-0.009}$	$166^{+19+8}_{-15-8}$	$-2.60^{+0.13+0.15}_{-0.21-0.40}$	$0.987^{+0.003}_{-0.004}$	$8.03^{+0.03}_{-0.03}$	119.03
103008010	2008/09/01	54710	$-2.105^{+0.005+0.013}_{-0.005-0.007}$	$148^{+14+1}_{-51-8}$	$-2.32^{+0.12+0.06}_{-0.08-0.14}$	$0.979^{+0.003}_{-0.003}$	$8.05^{+0.03}_{-0.03}$	139.51
104001010	2009/04/02	54922	$-2.103^{+0.007+0.000}_{-0.007-0.006}$	$111^{+13+0}_{-11-0}$	$-2.25^{+0.03+0.00}_{-0.04-0.07}$	$0.969^{+0.003}_{-0.003}$	$7.97^{+0.04}_{-0.04}$	107.22
104001070	2010/02/23	55250	$-2.123^{+0.011+0.000}_{-0.008-0.064}$	$173^{+171+0}_{-64-76}$	$-2.26^{+0.13+0.06}_{-0.79-0.38}$	$0.949^{+0.005}_{-0.005}$	$7.71^{+0.05}_{-0.05}$	86.83
105002010	2010/04/05	55291	$-2.124^{+0.006+0.000}_{-0.006-0.159}$	$145^{+27+0}_{-26-89}$	$-2.26^{+0.06+0.12}_{-0.09-0.19}$	$0.950^{+0.003}_{-0.003}$	$7.71^{+0.03}_{-0.04}$	130.47
105029010	2011/03/21	55641	$-2.133^{+0.005+0.011}_{-0.005-0.005}$	$247^{+30+0}_{-19-143}$	$-1.44^{+0.35+0.20}_{-0.22-0.57}$	$0.958^{+0.003}_{-0.003}$	$7.73^{+0.03}_{-0.03}$	111.70
106012010	2011/09/01	55805	$-2.117^{+0.007+0.005}_{-0.007-0.006}$	$108^{+34+475}_{-15-93}$	$-2.20^{+0.03+0.06}_{-0.05-0.07}$	$0.965^{+0.003}_{-0.003}$	$7.87^{+0.04}_{-0.05}$	97.46
106013010	2012/02/28	55986	$-2.173^{+0.023+0.034}_{-0.035-0.000}$	$45^{+10+242}_{-12-0}$	$-2.11^{+0.01+1.15}_{-0.01-0.28}$	$0.954^{+0.006}_{-0.005}$	$7.69^{+0.09}_{-0.06}$	100.32
106014010	2012/03/14	56001	$-2.125^{+0.005+0.008}_{-0.005-0.009}$	$166^{+17+6}_{-15-6}$	$-2.54^{+0.11+0.13}_{-0.15-0.28}$	$0.970^{+0.003}_{-0.003}$	$7.87^{+0.03}_{-0.03}$	103.74
106015010	2012/03/26	56012	$-2.133^{+0.007+0.009}_{-0.007-0.010}$	$173^{+18+4}_{-17-8}$	$-2.74^{+0.18+0.16}_{-0.25-0.34}$	$0.970^{+0.004}_{-0.004}$	$7.83^{+0.04}_{-0.04}$	128.49

Values of the first errors of  $\Gamma_1$ ,  $E_{break}$  and  $\Gamma_2$  are statistical errors at 90% confidence levels. Each sum of two values of errors represents the sum of statistical and systematic errors of the GSO NXB (1%; see text) at 90% confidence levels.

\* in unit of  $\times 10^{-8}$  erg cm $^{-2}$  s $^{-1}$  at 25–55 keV

† in unit of  $\times 10^{-9}$  erg cm $^{-2}$  s $^{-1}$  at 50–100 keV

‡ d.o.f. = 85.

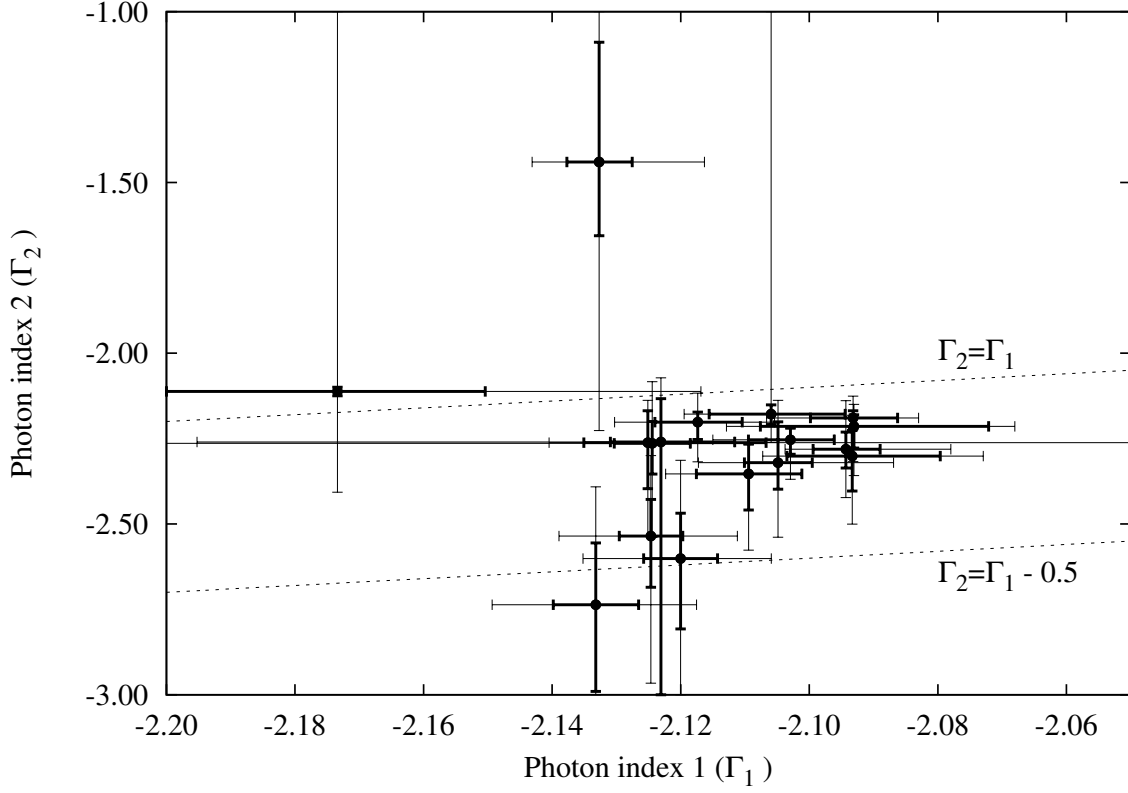


**Fig. 6.**  $\Gamma_1$  vs.  $\Gamma_2$  plots of the best-fit broken power-law models for individual spectra. The small error bars (bold lines) represent statistical errors and the large error bars (fine lines) represent systematic errors of the NXB uncertainty (see text). All errors are on a 90% confidence level.

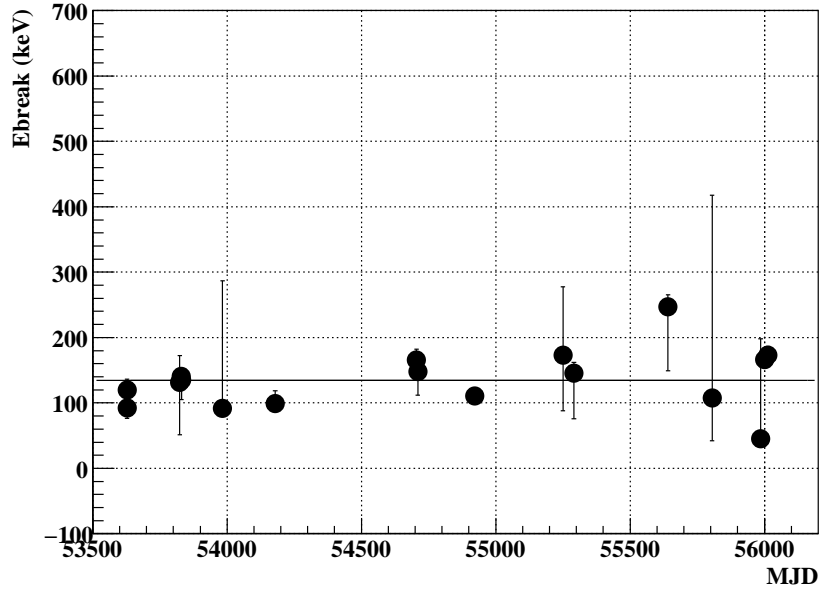


**Fig. 7.** Time (MJD) vs.  $E_{break}$  of the best-fit broken power-law models for individual spectra. The error bars represent statistical errors plus systematic errors of the NXB uncertainty (see text). All errors are on a  $1\sigma$  level. The solid line represents the best-fit constant function.

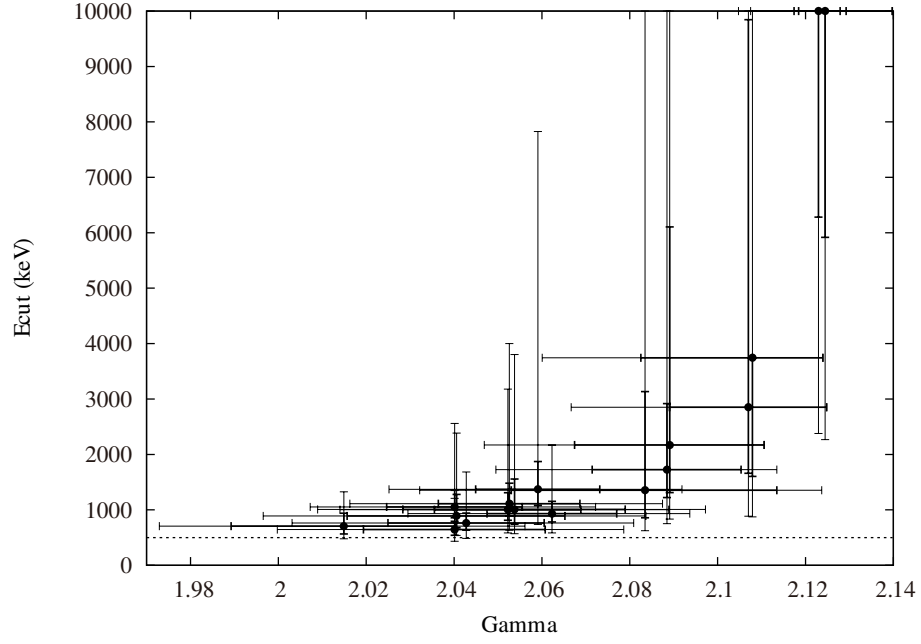


**Fig. 8.**  $\Gamma$  vs.  $E_{cut}$  of the best-fit cutoff power-law models for individual spectra. The dashed line shows  $E_{cut} = 500$  keV. The small error bars (bold lines) represent statistical errors; the large error bars (fine lines) represent systematic errors of the NXB uncertainty (see text). All errors are on a 90% confidence level.



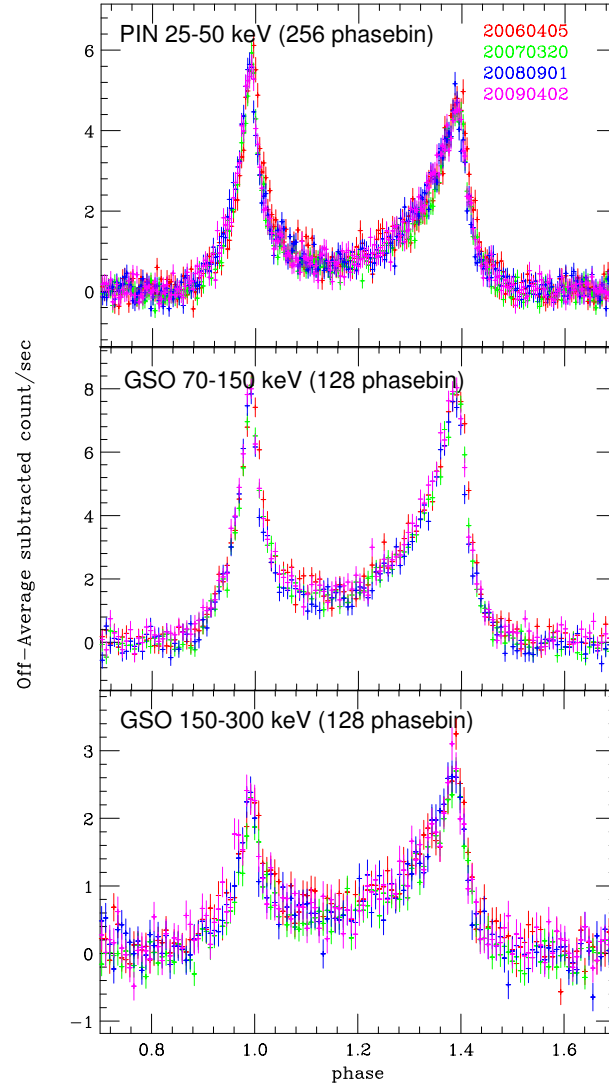


**Fig. 9.** Pulse profiles of the Crab pulsar observed with the HXD nominal position. Vertical axes show the count rates with subtraction of the average Off phase values. The error bars represent statistical errors ( $1\sigma$ ).

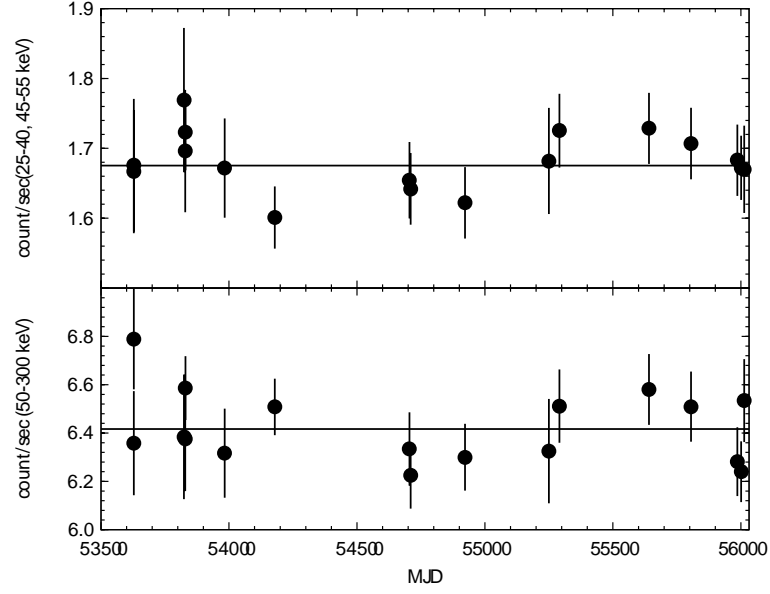


**Fig. 10.** Count rates of the Pulsed components of the Crab pulsar in 25–40, 45–55 keV of the PIN (top) and in 50–300 keV of the GSO (bottom). The dashed line in each panel represents the best-fit constant function in each energy band. All errors are on a 90% confidence level.